RSC Advances

PAPER

View Article Online
View Journal | View Issue

Cite this: *RSC Adv.*, 2026, **16**, 5707

Reverse micelle synthesis and downsizing effects in iron(III) spin crossover materials

Sharon E. Lazaro, [a] Phimphaka Harding, [b] Upsorn Boonyang, [c] Shane G. Telfer, [d] Wasinee Phonsri, [e] Keith S. Murray [e] and David J. Harding *[b]

Received 26th September 2025
Accepted 22nd January 2026

DOI: 10.1039/d5ra07308a

rsc.li/rsc-advances

We report the reverse micelle synthesis, structural characterisation and magnetic properties of iron(III) spin crossover (SCO) nanomaterials based on $[Fe(qsal)_2]NO_3$, $[Fe(qsal\text{-}I)_2]OTf$ and $[Fe(qsal\text{-}I)_2]NTf_2$ using sodium dioctylsulfosuccinate (NaAOT) and hexane. The synthesis and characterization of a new complex, $[Fe(qsal)_2]NO_3 \cdot EtOH$ is also reported. Systematic variation of micellar conditions including surfactant content in the polar and organic phases, reaction time, and solvent choice enabled the controlled formation of parallelogram, plate-like and rod-like shapes for $[Fe(qsal)_2]NO_3$, $[Fe(qsal\text{-}I)_2]OTf$ and $[Fe(qsal\text{-}I)_2]NTf_2$, respectively, as confirmed by FESEM. Magnetic studies reveal abrupt spin crossover with a narrower hysteresis width compared to the bulk materials. Nanomaterials of $[Fe(qsal\text{-}I)_2]OTf$ exhibit a 4 K hysteresis ($T_{1/2}\uparrow$ = 231 K and $T_{1/2}\downarrow$ = 227 K) while those of $[Fe(qsal\text{-}I)_2]NTf_2$ display a 27 K hysteresis ($T_{1/2}\uparrow$ = 275 K and $T_{1/2}\downarrow$ = 248 K) comparable to the bulk. The results demonstrate that reverse micelle methods can reliably produce iron(III) SCO nanomaterials, advancing their potential for integration into functional devices.

Introduction

A long-standing goal in spin crossover (SCO) chemistry is the synthesis of magnetic nanomaterials for integration into miniature functional and electronic devices. While the effects of size reduction on magnetic materials are well-documented, research regarding SCO materials remains comparatively limited.[1–3] Nevertheless, downsizing of these systems is highly desirable, as it can lead to rapid switching and enhanced memory storage capabilities.[4–6] To date, synthetic strategies such as rapid precipitation and reverse microemulsion[7,8] have been used to produce spin crossover nanoparticles (SCO NPs) of varied sizes and shapes. However, most research has focused on only two systems, the 1D triazole $[Fe(Rtrz)_3](A)_2$ {R = H, NH_2; A = anion} and the 3D systems $[Fe(pz)\{M(CN)_4\}]$ (M = Ni, Pt, Pd). Representative examples include $[Fe(Htrz)_2trz]BF_4$,[9,10] $[Fe(Htrz)_2(trz)](BF_4)\cdot H_2O$,[11–13] $[Fe(NH_2trz)_3](tosylate)_2$,[14,15] $[Fe(NH_2trz)_3]Br_2\cdot 3H_2O$[16] and $[Fe(pz)\{Ni(CN)_4\}]$,[17] which have been successfully processed into thin films,[18–20] composites[21] and hybrid materials.[22–24] Reverse micelle synthesis has also been applied to $[Fe(Htrz)_2(trz)](BF_4)@SiO_2$ with the NPs showing robust SCO properties.[25,26] Similarly, naked $[Fe(NH_2\text{-}trz)_3](NO_3)_2$ and core@shell $[Fe(NH_2trz)_3](NO_3)_2@SiO_2$ nanoparticles which showed a 7 K thermal hysteresis width near room temperature and sizes ranging from *ca.* 60 and 40 nm were also reported.[27]

In 2007, Coronado and his group used NaAOT (dioctyl sodium sulfosuccinate) and octane in a reverse microemulsion to synthesize *ca.* 10 nm-diameter $[Fe(Htrz)_2(trz)](BF_4)$ SCO NPs with a narrow size distribution which maintained a 40 K hysteresis width,[27] similar to the bulk material. Using a similar method, SCO NPs of $[Fe(Htrz)_2(trz)](BF_4)\cdot H_2O$ with different sizes (4, 12 and 18 nm) were produced by varying the water to surfactant ratio. This also showed a significant decrease in hysteresis width as the size of the NPs is reduced.[11] Rod-shaped NPs of $[Fe(Htrz)_2trz]BF_4$ synthesized using NaAOT and behenic acid were reported by Roubeau *et al.* revealing that an increase in the rod width is directly proportional to an increase in the hysteresis width,[9] while the removal of surfactant from the raw nanoparticles decreased the hysteresis.

Our group has been actively exploring iron(III) complexes, some with remarkable SCO characteristics.[28] However, to the best of our knowledge, only one iron(III) complex has been explored and synthesized as nanomaterials. In this case, abrupt precipitation in 1-butanol produced needle-shaped microcrystals and spherical NPs of $[Fe(salEen\text{-}3\text{-}OMe)_2]PF_6$. PEG

[a]*Functional Inorganic Materials Laboratory, Department of Chemistry, College of Science, Central Luzon State University, Science City of Munoz, Nueva Ecija, 3120, Philippines*

[b]*School of Chemistry, Institute of Science, Suranaree University of Technology, Nakhon Ratchasima, 30000, Thailand. E-mail: david@g.sut.ac.th*

[c]*Walailak University, 222 Thaiburi, Thasala, Nakhon Si Thammarat 80160, Thailand*

[d]*MacDiarmid Institute for Advanced Materials and Nanotechnology, Institute of Fundamental Sciences, Massey University, New Zealand*

[e]*School of Chemistry, Monash University, Clayton, Melbourne, Victoria, 3800, Australia*

(polyethylene glycol) was used to confine and control the size and growth of the 18 nm spherical spheres.[29] The small hysteresis in the bulk material disappeared when nanosized and a shift in the transition temperature, from 162 K in the bulk to 153 K in the 18 nm particles, was observed. Nanorods of the same complex prepared and embedded into a thin film of PVP {poly(vinyl)pyrrolidone} showed an increased LS to HS transition using light.[30,31] With these promising results, further studies on transforming SCO complexes of iron(III) into nanomaterials is clearly of value to widen their applications.

To address this need for reproducible synthetic routes to molecular SCO nanomaterials we report the synthesis, characterization and magnetic properties of a new molecular SCO material $[Fe(qsal)_2]NO_3 \cdot EtOH$ **1**, and nanomaterials of $[Fe(qsal)_2]NO_3$ **2**, $[Fe(qsal\text{-}I)_2]OTf$ **3**, and $[Fe(qsal\text{-}I)_2]NTf_2$ **4**. The molecular complexes, **3** and **4** were chosen as both exhibit abrupt SCO but have narrow, 8 K and wide hysteresis, 34 K, respectively.[32,33] By investigating the influence of surfactant concentration, solvent choice and reaction time we demonstrate that these molecular complexes can be effectively downsized. Moreover, our findings reveal a divergence in performance: while systems with narrow hysteresis show reduced magnetic performance upon downsizing, strongly hysteretic systems maintain their SCO behaviour. This represents the first time this has been reported in a molecular SCO system.

Results and discussion

To allow us to study the various effects and applicability of reverse micelle synthesis we began with a simpler system, $[Fe(qsal)_2]NO_3$. Surprisingly, $[Fe(qsal)_2]NO_3$ has only been reported as an intermediate and the structure of the compound is unknown. Hence, we synthesized the compound as the ethanol solvate which allowed us to compare the magnetic properties of the bulk and nanomaterials.

Synthesis and basic characterization of $[Fe(qsal)_2]NO_3 \cdot EtOH$ 1

The molecular complex **1** was synthesized by layering a solution of $Fe(NO_3)_3$ in EtOH over a solution of salicylaldehyde and 8-aminoquinoline in CH_2Cl_2 with NEt_3 (see Scheme S1). Ethanol was used as a buffer layer and black crystals were obtained after 5 days. IR spectroscopic analysis revealed stretches at 3406, 1602 and 1383 cm^{-1} which correspond to the O–H, C=N and nitrate anion, respectively (Fig. S1). The UV-vis spectrum was recorded in CH_2Cl_2 with absorption bands at 331 (ε = 11 800 $dm^3\ mol^{-1}\ cm^{-1}$) and 411 nm (ε = 6700 $dm^3\ mol^{-1}\ cm^{-1}$) indicative of the π–π transition and the ligand to metal charge transfer (LMCT), respectively. The IR stretch for the NO_3^- anion is similar to that found in $[Fe(qsal\text{-}I)_2]NO_3 \cdot 2ROH$ (R = Me or Et).[28]

Crystallographic data of **1** (Table 1) collected at 293 K shows that it crystallizes in the triclinic space group $P\bar{1}$ with a $[Fe(qsal)_2]^+$ cation, nitrate anion and a molecule of ethanol in the asymmetric unit. The iron(III) center is six-coordinate with four nitrogen atoms and two oxygen atoms from two qsal ligands. The average Fe–O/Fe–N bond lengths are 1.885(1) and 1.951(2) Å, typical of a low spin iron(III) center.

Two π–π interactions, 3.603(6) and 3.756(5) Å between the aromatic rings of the quinoline and the salicylaldimine groups of the ligand dominate the packing, as is typical in $[Fe(qsal\text{-}X)_2]^+$ systems.[34–38] Intermolecular C–H···O contacts between the aromatic ring and the NO_3^- anion are also present. The structure exhibits hydrogen bonding between the NO_3^- anion and the ethanol molecule in the lattice. Furthermore, the π–π interactions form a 1D chain where the iron(III) centers are all low spin with the nitrate anion serving as a link between the $[Fe(qsal)_2]^+$ units (Fig. 1 and S2).

Synthesis of $[Fe(qsal)_2]NO_3$ NPs

All nanomaterials (NMs) were synthesized using a reverse micelle procedure adapted from the literature with minor modifications.[7] Two surfactant solutions were prepared in separate flasks; each containing 2 g of NaAOT dissolved in 10 mL of *n*-hexane; although *n*-octane was also found to be effective. The Hqsal ligand was dissolved in MeCN and added to the first flask, while the iron precursor was prepared by adding an aqueous solution of $Fe(NO_3)_3$ to the second. Both flasks were stirred for 30 minutes yielding homogenous solutions, indicating the formation of stable reverse micelles.[7] The Hqsal-containing micellar solution was then slowly added to the Fe^{3+} solution which turned brown, with small brown particles

Table 1 Crystallographic data and structure refinement for $[Fe(qsal)_2]NO_3 \cdot EtOH$ at 293 K

Formula	$C_{34}H_{28}FeN_5O_6$	T/K	293
Molecular weight (g mol^{-1})	658.48	Absorption coefficient/mm^{-1}	4.703
Crystal system	Triclinic	2θ range for data collection/°	6.984 to 144.112
Space group	$P\bar{1}$	Index ranges	$-12 \le h \le 12$, $-14 \le k \le 14$, $0 \le l \le 15$
Z	2	Reflections collected	5398
a/Å	10.2636(11)	Independent reflections	5398
b Å	11.9494(11)	Restraints/parameters	35/434
c/Å	12.8936(12)	R_{int}, R_{sigma}	n/a, 0.1482
α/°	85.389(6)	R_1, wR_2 ($I \ge 2\sigma$)	0.1059, 0.2785
β/°	78.976(6)	Goodness-of-fit on F^2	1.066
γ/°	67.687(5)	Max. and min. transition	1.000/0.593
Cell volume/$Å^3$	1435.9(3)	Largest diff. peak/hole/e $Å^{-3}$	0.80/−0.70

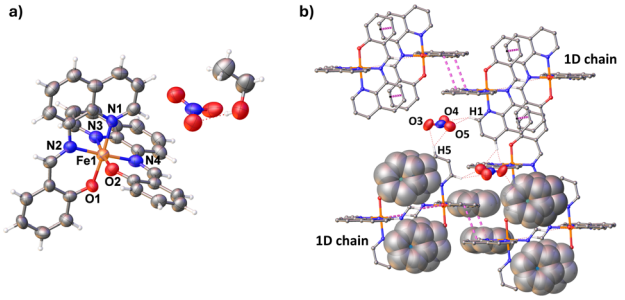

Fig. 1 (a) View of the asymmetric unit of **1** at 293 K and (b) π–π stacking between the aromatic moieties and C–H···O interactions between the NO_3^- anion and the $[Fe(qsal)_2]^+$ units.

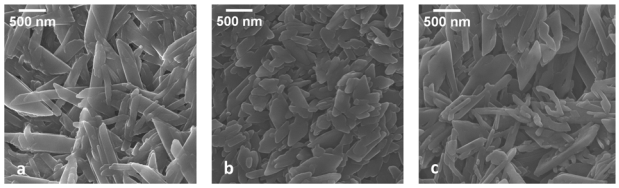

Fig. 3 FESEM images of $[Fe(qsal)_2]NO_3$ materials synthesized using (a) H_2O (b) EtOH and (c) MeOH as the solvent for the Fe^{3+} precursor. The Hqsal ligand and iron(III) micellar concentrations were fixed at 2.0 g of NaAOT.

beginning to form after 15 min (Fig. 2). After 24 h, the suspension was centrifuged to afford a dark brown residue. Residual surfactant was removed by redispersing the residue in EtOH and centrifuging again for 30 min. This was repeated three times resulting in dark brown solids. The final product was dried in air and subjected to morphological and size distribution analyses. FESEM images revealed stacked, parallelogram-shaped particles with dimensions of *ca.* 800 nm-2.6 μm × 200–800 nm × 60–200 nm in length, width and thickness (Fig. 3). This means that these materials sit on the border between the nano- and microscale, but as the width and thickness are well within the nanoscale we use the term nanomaterials to describe the materials reported here.[8]

To examine the influence of the Fe^{3+} precursor, ethanol and methanol were tested as alternatives to water (entries 1–3; Table 2). Both readily formed micellar solutions. FESEM images in Fig. 3 reveal that using ethanol produced smaller plate-like particles with average dimensions of 403 ± 57 nm (length) and 158 ± 68 nm (width). In contrast, methanol yielded parallelogram-shaped particles alongside deformed particles with central voids, suggesting incomplete formation or partial dissolution. This suggests that methanol is not a suitable solvent for making nanomaterials in this case.

Next, we systematically varied the reaction time from 1 to 48 hours (Fig. S3). After 1 h, the resulting solids had no defined morphology. Parallelogram-shaped NMs started to form after four hours, however FESEM micrographs and size distribution data showed that 24 h is the optimal time for the complete formation of the NMs. Stirring for 48 h resulted in longer NMs with an average size of 1855 ± 735 nm. As might be expected, the yield of reaction was considerably reduced at shorter reaction times.

To explore the effect of surfactant concentration the amount of NaAOT in the organic phase (MeCN) was varied (0.5, 1, 2 and 4 g; entries 4–7 in Table 2), while maintaining 2 g of NaAOT in

Table 2 Experimental conditions used in the synthesis of nanomaterials of $[Fe(qsal)_2]NO_3$

Entry	Amount of NaAOT (ligand solution)	Amount of NaAOT (metal solution)
1	2 g	2 g
2	2 g	2 g (EtOH)
3	2 g	2 g (MeOH)
4	0.5 g	2 g
5	1 g	2 g
6	2 g	2 g
7	4 g	2 g
8	2 g	0.5 g
9	2 g	1 g
10	2 g	2 g
11	2 g	4 g
12	0.5 g	0.5 g
13	1 g	1 g
14	2 g	2 g
15	4 g	4 g

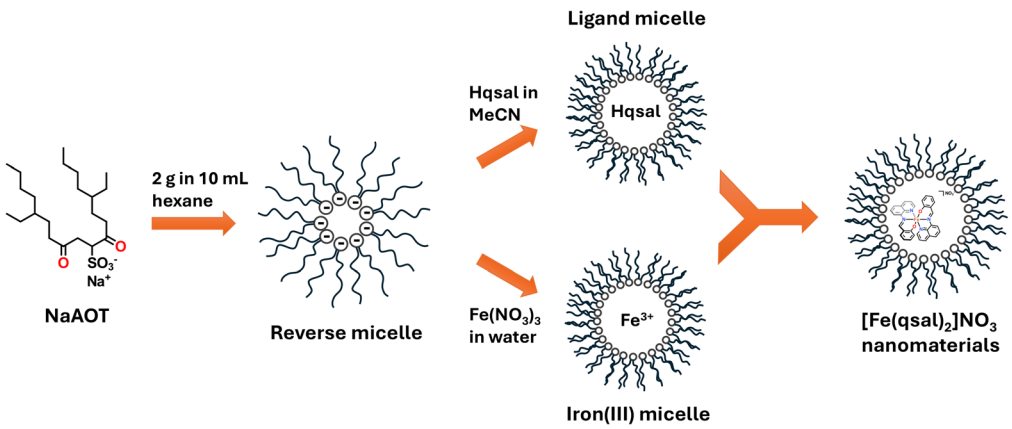

Fig. 2 Visual representation of the reverse micelle synthesis of the $[Fe(qsal)_2]NO_3$ nanoparticles.

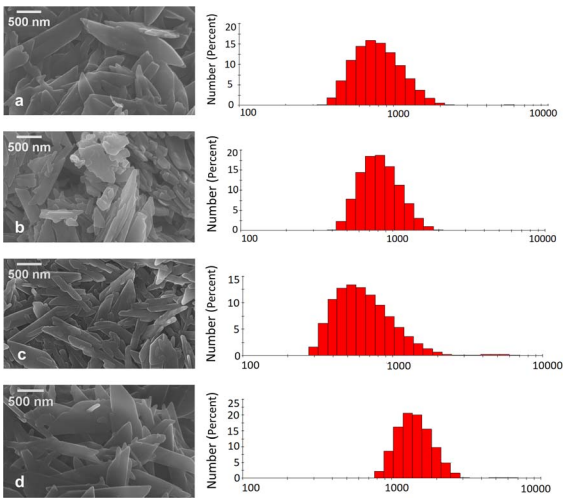

Fig. 4 FESEM images and DLS size distribution graphs of $[Fe(qsal)_2]NO_3$ materials synthesized using (a) 0.5 g (b) 1.0 g (c) 2.0 g and (d) 4.0 g of NaAOT in MeCN for the ligand micelle solution. The iron(III) micellar concentration is fixed at 2.0 g of NaAOT.

all Fe^{3+} micellar solutions. DLS measurements revealed that 2 g of NaAOT produced the smallest particles with an average hydrodynamic diameter of 924 ± 11.5 nm. The average diameters for systems containing 0.5, 1 and 4 g of NaAOT were 975 ± 29, 1061 ± 30 and 1774 ± 138 nm, respectively (Fig. 4).

In a complementary experiment, the NaAOT content in the Fe^{3+} micellar solutions was varied while keeping the ligand micellar solution constant at 2 g NaAOT (Fig. 5; entries 8–11 in Table 2). Of these the 2 g : 1 g ratio of NaAOT in the organic and aqueous phases produced the smallest particles with the narrowest size distribution, but with reduced overall yield. Increasing the NaAOT concentration to 4 g once again produced longer particles with an average size of 1775 ± 90.2 nm.

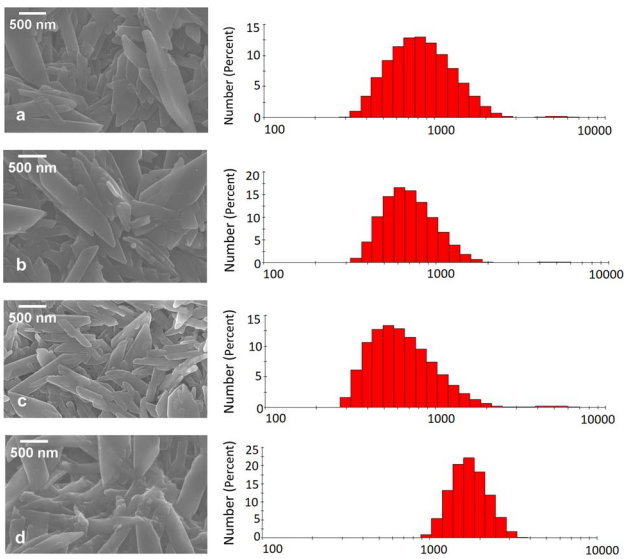

Fig. 5 FESEM images and DLS size distribution graphs of $[Fe(qsal)_2]NO_3$ materials synthesized using (a) 0.5 g (b) 1.0 g (c) 2.0 g and (d) 4.0 g of NaAOT in water for the iron(III) micelle solution. The ligand micellar concentration is fixed at 2.0 g of NaAOT.

In a final experiment we fixed the ratio between the organic and aqueous phases to be 1 : 1 (see entries 12–15 in Table 2). At 2 g of NaAOT and below, the particles are parallelogram shaped with the size of the nanoparticles smallest when 2 g of NaAOT was used for both phases (Fig. S4). In the 4 g NaAOT system, while the DLS measurements indicate particles with a narrow size distribution, the FESEM images indicate that the particles are poorly defined.

Previous studies on related systems, including $[Fe(Rtrz)_3](A)_2$ {R = H, NH_2; A = anion}[11] and $[Fe(phen)_2(NCS)_2]$[8] have established that particle size depends strongly on the water-to-surfactant ratio (ω_0). Nanoparticles of $[Fe(phen)_2(NCS)_2]$ were obtained at $\omega_0 = 3.6$ but initial experiments conducted at $\omega_0 = 5$ resulted in incomplete crystallization and low yield.[8] On the other hand, $[Fe(Htrz)_2(trz)](BF_4)\cdot H_2O$ NPs with different sizes were obtained at different ω_0.[11] Values of ω_0 = 5–6.5 produced 4 ± 2 nm NPs while at ω_0 = 7–9 nanoparticles 15 ± 5 nm. Both studies used only water to dissolve the starting materials. In the $[Fe(qsal)_2]NO_3$ system, the ω_0 ratio cannot be used to interpret the effect of NaAOT concentration on the particle sizes because of the different solvents required to dissolve the ligand and the iron precursors, as the Hqsal and Hqsal-X ligands are insoluble in water. However, our results show a clear trend: increasing the concentration of NaAOT leads to the formation of larger particles. Higher NaAOT concentrations strengthen interactions between the surfactant tails and organic solvent, resulting in a more stable micellar system. This enhanced stability reduces intermicellar exchange, thereby promoting the growth of larger particles.[39–42]

Synthesis and characterization of $[Fe(qsal\text{-}I)_2]OTf$ NPs 3 and $[Fe(qsal\text{-}I)_2]NTf_2$ NPs 4

Nanomaterials of **3** and **4** were synthesized based on the optimum conditions found in **2**; 2 g of NaAOT in both organic and polar phases, 24 h of stirring and washing with EtOH. However, differences in the solubility of Hqsal and Hqsal-I led us to explore other solvent systems capable of dissolving Hqsal-I and forming a stable micellar solution. Careful screening revealed that DMF (dimethylformamide) is a suitable solvent to dissolve Hqsal-I. Hence for the synthesis of **3** we dissolved the Hqsal-I in DMF and the Fe^{3+} precursor in MeCN. $FeCl_3$ was first dissolved in MeCN and KOTf was added to the solution to form $Fe(OTf)_3$ *in situ*. Subsequent mixing of the ligand and Fe^{3+} solution gave black solids which were isolated by centrifugation and washed with EtOH. FESEM images revealed plate-like aggregates. The thin plates seem to adhere to each other, with visible boundaries between the stacked layers (Fig. 5a). A similar solvent combination was used in the preparation of **4**. The Fe^{3+} precursor was prepared by dissolving $FeCl_3$ in MeCN followed by addition of $LiNTf_2$ prior to introducing it into the surfactant solution. Fine, black solids were obtained after washing with EtOH. FESEM micrographs revealed rod-like particles measuring *ca.* 100 nm–3 μm long and smaller widths and thicknesses, mirroring the morphology of the bulk crystals. DLS measurements revealed average hydrodynamic diameters of 510 ± 27 nm for **3** and 710 ± 193 nm for **4** (Fig. 5a and b). These are a little smaller than those observed in **2** and probably reflect the

lower solubility of the molecular complexes $[Fe(qsal\text{-}I)_2]OTf$ and $[Fe(qsal\text{-}I)_2]NTf_2$, compared with **1**. It is also noteworthy that while the nanoparticles in **3** have a poorly defined morphology, those of **4** are clearly rod-like with more well-defined edges possibly suggesting a higher degree of crystallinity (Fig. S5).

To further characterize the nanomaterials IR spectroscopic studies of **1–4** were undertaken which show C=N stretches at 1599–1603 cm^{-1} for the imine bond. C–F stretches at 1138–1139 cm^{-1} for the CF_3 groups in the anions of **3** and **4** are also observed, while S–O bands for **3** and **4** are observed at 1030, 1260 and 1373 cm^{-1}, similar to where they are found in the bulk materials (Fig. S1).[32,33] The presence of these characteristic bands confirms that these are nanomaterials of the molecular complexes.

Powder X-ray diffraction data

The powder X-ray diffraction patterns of the bulk and nanomaterials of $[Fe(qsal\text{-}I)_2]OTf$ were compared to the calculated pattern of $[Fe(qsal\text{-}I)_2]OTf\cdot MeOH$ obtained at room temperature, Fig. S6. Peaks of **3** observed at 13.6, 15.8, 19.7 and 25.7° in the calculated diffractogram are shifted to higher angles by about 1–2° compared with the bulk material. This difference is likely due to the loss of solvent in the nanomaterial sample, as confirmed by elemental analysis. Similarly, the 2θ values of the bulk material of **4** are about 0.3–1.0° higher than the peak positions observed in the nanomaterials and the calculated diffractogram. The close similarity between bulk and nanomaterials of **3** and **4** under the same experimental conditions and relatively sharp peaks in the diffractogram suggest the nanomaterials retain their crystallinity upon downsizing. In both cases, the PXRD are consistent with the products being nanomaterials of **3** and **4**. This is consistent with the literature on $[Fe(NCS)_2(phen)_2]$[8] and $[Fe(AP\text{-}Mesal)_2]$[43] (AP-Mesal = 2-hydroxy-3-methyl-*N*′-((pyridin-2-yl)-ethylidene)benzohydrazide) which shows that downsizing causes only a slight loss in crystallinity.

Magnetic studies

Magnetic studies on all samples were conducted using SQUID magnetometry and are presented as $\chi_M T$ *versus* T plots in Fig. 7 and 8. Both **3** and **4** exhibit abrupt spin crossover with hystereses similar to the bulk materials.[32,33] For **3**, at 50 K, $\chi_M T$ is found to be 1.20 $cm^3\ mol^{-1}$ K, suggesting the compound is

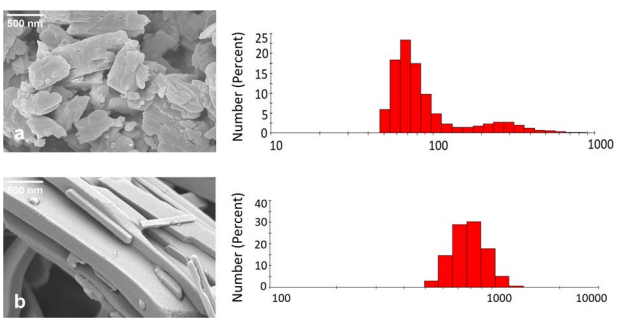

Fig. 6 FESEM images and DLS size distribution graph for (a) **3** and (b) **4** using a concentration of 2 g of NaAOT in both the ligand and iron(III) micellar phases.

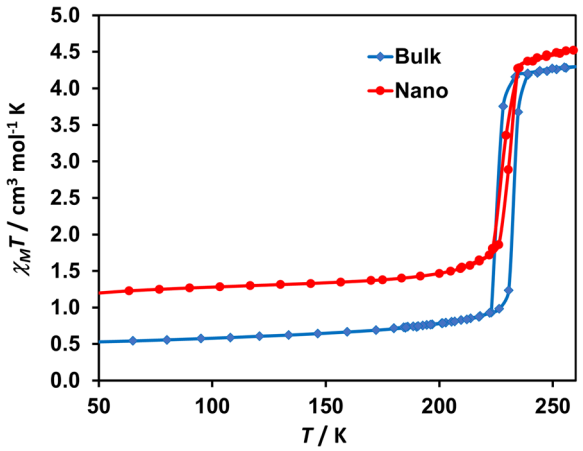

Fig. 7 $\chi_M T$ *versus* T plot of the bulk and nanomaterials of [Fe(qsal-I)]OTf.

mostly LS iron(III), with a residual amount of the sample HS, calculated to be 19% in NMs and 0.53% in the bulk (assuming $\chi_M T = 0.50\ cm^3\ mol^{-1}$ K for the LS state). A gradual increase was observed up to 230 K followed by an abrupt increase to 4.66 $cm^3\ mol^{-1}$ K at 310 K and consistent with HS Fe(III). The hysteresis width is $\Delta T = 4$ K where $T_{1/2}\uparrow = 231$ K and $T_{1/2}\downarrow = 227$ K (Fig. 7), and narrower than the 8 K hysteresis width observed in the bulk material ($T_{1/2}\uparrow$ = 232 K, $T_{1/2}\downarrow$ = 224 K).[32] This result is commonly observed in nanosized SCO complexes.[8,29,43,44] The narrower hysteresis width suggests reduced cooperativity likely due to diminished long-range interactions as the particles become smaller. The higher HS fraction in the nanomaterial can be attributed to the Fe^{3+} ions located on the surface of the NMs where trace amounts of the surfactant may prevent spin crossover.[11,45]

The magnetic profile of **4** (Fig. 8) closely resembles the bulk material but with a slightly narrower hysteresis width. A gradual increase up to 270 K is observed from a starting $\chi_M T$ value of 0.49 $cm^3\ mol^{-1}$ K which increases abruptly to 4.26 $cm^3\ mol^{-1}$ K at 350 K. This time we observe a complete and reversible SCO.

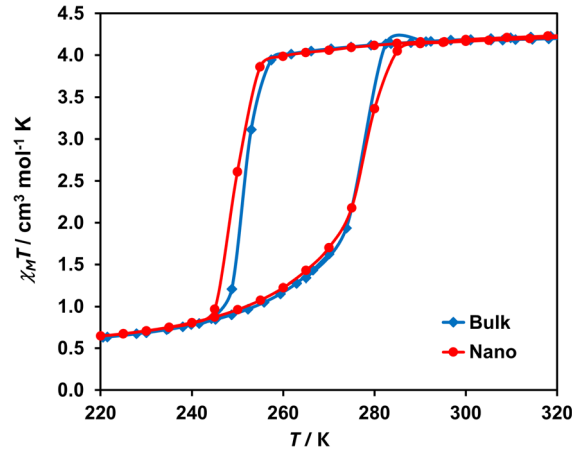

Fig. 8 $\chi_M T$ *versus* T plots of the bulk and nanomaterials of **4**.

The warming mode shows $T_{1/2}\uparrow = 275$ K, while in the cooling mode $T_{1/2}\downarrow = 248$ K resulting in a hysteresis of 27 K which is 3 K lower than the bulk material. This is reproducible as proven by using 2, 5 and 10 K min^{-1} cycling rate (Fig. S7). In contrast to **3**, the %HS residue in the NMs of **4** remains low and is comparable with the bulk material. This is similar to the findings in $[Fe(3\text{-}OMe\text{-}SalEen)_2]PF_6$ with *ca.* 5% HS residue in the 18 nm NPs.[29] This is thought to be due to the crystallinity of the particles which was maintained even in the smallest NPs.

Similarly, the NMs of **4** are also crystalline even when nanosized (see Fig. 6b), probably as they do not contain a solvent of crystallization. In contrast to $[Fe(salEen\text{-}3\text{-}OMe)_2]PF_6$, the abrupt SCO is preserved, but this may be due to the larger size of the nanomaterials in this study, or because of the more robust packing that is generally observed in $[Fe(qsal\text{-}X)_2]^+$ complexes.[34–38] Further work is clearly required to disentangle the various factors at play in the downsizing of molecular SCO complexes. Neither bulk nor nanomaterials of $[Fe(qsal)_2]NO_3$ exhibit significant SCO. The bulk material shows very slight SCO from 0.45 cm^3 mol^{-1} K at 100 K to 1.03 cm^3 mol^{-1} K at 350 K. A slightly higher $\chi_M T$ value of 1.21 cm^3 mol^{-1} K at the same temperature for the nanomaterial also reveals gradual and incomplete SCO. Similar results are obtained in the nanomaterials prepared using different amounts of NaAOT and at different reaction times (Fig. S8). The lack of substantial SCO in **1** is likely due to the tight packing in the complex that prevents the expansion required to access the HS state.[34]

Conclusions

In conclusion, we have successfully employed the reverse micelle technique to synthesise nanomaterials of the iron(III) SCO complexes $[Fe(qsal)_2]NO_3$, $[Fe(qsal\text{-}I)_2]OTf$ and $[Fe(qsal\text{-}I)_2]NTf_2$. Through systematic optimization of surfactant concentration, solvent choice and reaction time, we demonstrated control over particle morphology, resulting in distinct parallelogram, plate and rod-like nanomaterials. Magnetic susceptibility studies reveal that the nanomaterials retain their SCO characteristics, with only a minor reduction in thermal hysteresis widths from 8 K to 4 K for **3** and 30 K to 27 K for **4**. Interestingly, the highly crystalline, rod-like particles of **4** exhibited a low residual HS fraction, whereas the less defined aggregates of **3** showed a 19% residual fraction, attributed to surface effects. These results confirm that reverse micelle synthesis is a reliable route to iron(III) SCO nanomaterials that preserve their magnetic cooperativity. Further work will explore temperature and more confining surfactants with the aim of producing even smaller nanoparticles to better understand nanosizing effects on molecular SCO complexes.

Methodology

General remarks

Reagents and solvents, except Hqsal and Hqsal-I,[46] were purchased from Sigma-Aldrich or TCI Chemicals and used as received. Infrared spectra (as KBr discs) were recorded on a Bruker Tensor 27 FTIR in the range of 400–4000 cm^{-1}. Electronic spectrum of $[Fe(qsal)_2]NO_3 \cdot EtOH$ was recorded in DCM at room temperature on an Avantes Fiber Optics Spectrometer with Avalight-DHC and Avaspec ULS2048XL-USB2 in the range of 200–1000 nm. The morphology and size of the nanoparticles were determined using JEOL JSM-7001 F Zeiss Supra 55 VP Zeiss Merlin Compact FESEM operated at 3–5 KV. Samples were placed on a carbon tape and coated with carbon. Size distribution was determined using a Malvern Zetasizer Nano Series analyzer. Ethanol was used to dissolve the NPs and the measurement was done at 25 °C. Elemental analysis and ESI-mass spectrometric analyses of $[Fe(qsal)_2]NO_3 \cdot EtOH$ and the nanomaterials was performed at the Elemental Analysis Laboratory, National University of Singapore.

X-ray crystallography

Crystallographic data for $[Fe(qsal)_2]NO_3 \cdot EtOH$ are given in Table 1. Crystals were grown by layering an ethanol solution of $Fe(NO_3)_3$ over a solution of Hqsal and NEt_3 in CH_2Cl_2. Crystals were mounted on a glass fibre using perfluoropolyether oil. Diffraction data were collected using Rigaku Spider diffractometer equipped with a MicroMax MM007 rotating anode generator, Cuα radiation (λ = 1.54178 Å), high-flux Osmic multilayer mirror optics, and a curved image-plate detector.[47] The structures were then solved by direct methods and refined on all F^2 data using SHELXT[48] and SHELXL.[49] The structure was found to be twinned and modeled as 91.9/8.1 major and minor components, respectively. Non-hydrogen atoms were refined with anisotropic thermal parameters; hydrogen atoms were included in calculated positions and refined with isotropic thermal parameters which were 1.2 × (aromatic CH) or 1.5 × (Me, CH_2, OH) the equivalent isotropic thermal parameters of their parent carbon atoms. All pictures were generated with OLEX2.[50]

Powder XRD

Powder X-ray diffraction patterns were recorded using a Rigaku Oxford Diffraction XtaLAB Supernova diffractometer equipped with a Hypix-3000 photon counting detector and a Cu radiation source (λ = 1.54184 Å). The samples were suspended in perfluoropolyether oil and the data collected in powder diffraction mode.

Magnetic susceptibility studies

Magnetic studies were done using a Quantum Design MPMS 5 SQUID magnetometer under an applied field of 1 T over the temperature range of 50–360 K for **1**, 50–310 K for **2** and 100–350 K for **3** and **4**. Crystalline samples of **1** and powdered samples for all nanomaterials were used for the analyses.

Synthesis of $[Fe(qsal)_2]NO_3 \cdot EtOH$ crystals

Layered diffusion was used to prepare the $[Fe(qsal)_2]NO_3 \cdot EtOH$ crystals. Salicylaldehyde (0.21 mL, 2 mmol) and 8-aminoquinoline (288.4 mg, 2 mmol) were dissolved in DCM with NEt_3 and layered at the bottom of a test tube. A buffer layer of EtOH (2 mL) was placed in the middle. $Fe(NO_3)_3 \cdot 9H_2O$ (404 mg,

1 mmol) was dissolved in EtOH and layered over it. Black crystals were obtained after 5 days and filtered yielding 528.5 mg (86%). ν_{max}(KBr)/cm^{-1} 3406 (ν_{OH}), 1602 ($\nu_{C=N}$), 1382 (ν_{anion}). λ_{max}(DCM)/nm (ε, dm^3 mol^{-1} cm^{-1}) 331 (11 800), 411 (6700). Calc. for (found %) $C_{32}H_{26}FeN_5O_5$: C, 62.76 (62.64); H, 3.62 (3.62); N, 11.40 (11.29).

Synthesis of [Fe(qsal)$_2$]NO$_3$ NMs

Time, solvent choice and the concentration of the surfactant were all explored in this research. The experimental details for the standard protocol are given below.

Two flasks were prepared, each containing 2 g of NaAOT dissolved in 10 mL of hexane. Hqsal (49.7 mg, 0.2 mmol) was dissolved in MeCN (0.3 mL) and added to the first flask while $Fe(NO_3)_3 \cdot 9H_2O$ (40.4 mg, 0.1 mmol) was dissolved in water (0.3 mL) and added to the second flask. Both flasks were stirred for 30 min to obtain stable micellar solutions. The ligand solution was slowly added to the Fe^{3+} solution and stirred for 24 h. It was then centrifuged at 5000 rpm for 30 min. The solids were washed three times by redispersing the solids in EtOH and centrifuged for another 30 min. Dark brown powder was obtained after drying in air. ν_{max}(KBr)/cm^{-1} 3442 (ν_{OH}), 1603 ($\nu_{C=N}$), 1383 (ν_{anion}). Calc. for (found %) $C_{32}H_{26}FeN_5O_5$: C, 62.76 (62.53); H, 3.62 (3.75); N, 11.40 (11.14).

A summary of the different experimental conditions explored is shown in Table 2.

Synthesis of [Fe(qsal-I)$_2$]OTf NMs

Nanoparticles of **2** were prepared in a similar manner to **1** using Hqsal-I (74.6 mg, 0.2 mmol) dissolved in DMF (0.3 mL). The Fe precursor was prepared by dissolving $FeCl_3$ (16.2 mg, 0.1 mmol) in MeCN (0.3 mL) and adding KOTf (56.4 mg, 0.3 mmol). Black powder was obtained. ν_{max}(KBr)/cm^{-1} 3451 (ν_{OH}), 1599 ($\nu_{C=N}$), 1260 (ν_{S-O}), 1141 (ν_{C-F}), 1030 (ν_{S-O}). Calc. for (found %) $C_{33}H_{20}F_3FeI_2N_4O_5S$: C, 41.67 (41.32); H, 2.12 (2.28); N, 5.89 (5.77).

Synthesis of [Fe(qsal-I)$_2$]NTf$_2$ NMs

Nanoparticles of **3** were prepared in a similar manner to **1** using Hqsal-I (74.6 mg, 0.2 mmol) dissolved in DMF (0.3 mL). The Fe precursor was prepared by dissolving $FeCl_3$ (16.2 mg, 0.1 mmol) in MeCN (0.3 mL) and adding $LiNTf_2$ (86.0 mg, 0.3 mmol). Black powder was obtained. ν_{max}(KBr)/cm^{-1} 3440 (ν_{OH}), 1598 ($\nu_{C=N}$), 1373 ($\nu_{S=O}$), 1138 (ν_{C-F}). Calc. for (found %) $C_{34}H_{20}F_6FeI_2N_5O_6S_2$: C, 37.73 (37.98); H, 1.86 (1.95); N, 6.47 (6.32).

Author contributions

S. E. L: investigation, formal analysis, data curation, visualization, writing–original draft. P. H.: conceptualization, resources, writing–review and editing, supervision. U. B.: investigation, data curation. S. G. T.: investigation, data curation. W. P.: investigation, formal analysis, data curation. K. S. M.: investigation, formal analysis, data curation. D. J. H.: conceptualization, resources, writing–review and editing, supervision, funding acquisition.

Conflicts of interest

There are no conflicts to declare.

Data availability

The data that support the findings of this article can be obtained directly from the authors upon request. This includes additional FE-SEM images, raw data for the SQUID magnetometry measurements and the PXRD studies.

CCDC 2491569 (**1**) contains the supplementary crystallographic data for this paper.[51]

Supplementary information (SI): IR spectroscopic, structural figures, additional FESEM, PXRD and SQUID magnetometric data. See DOI: https://doi.org/10.1039/d5ra07308a.

Acknowledgements

This research has received funding support from the NSRF *via* the Program Management Unit for Human Resources & Institutional Development, Research and Innovation (grant number B39G680007). We gratefully acknowledge Suranaree University of Technology for partial financial support through the Molecular Magnetic Materials Research Unit.

Notes and references

1 Z. Shi, C. Fang, J. Li, S. Bandaru, M. Liu, L. Zhao and X. Zhang, Multi-Dimensional Design of Slippery Liquid-Infused Coatings Empowering Long-Term Corrosion Protection for Sintered Nd-Fe-B Magnets in Harsh Environments, *Small*, 2025, **21**, 2500629.
2 Q. Dong and Z. Jiang, Platinum–Iron Nanoparticles for Oxygen-Enhanced Sonodynamic Tumor Cell Suppression, *Inorganics*, 2024, **12**, 331.
3 Y. Zhao, Co-precipitated Ni/Mn shell coated nano Cu-rich core structure: A phase-field study, *J. Mater. Res. Technol.*, 2022, **21**, 546–560.
4 R. Torres-Cavanillas, M. Gavara-Edo and E. Coronado, Bistable Spin-Crossover Nanoparticles for Molecular Electronics, *Adv. Mater.*, 2024, **36**, 2307718.
5 S. Kamilya, B. Dey, K. Kaushik, S. Shukla, S. Mehta and A. Mondal, Realm of Spin State Switching Materials: Toward Realization of Molecular and Nanoscale Devices, *Chem. Mater.*, 2024, **36**, 4889–4915.
6 T. K. Ekanayaka, K. P. Maity, B. Doudin and P. A. Dowben, Dynamics of Spin Crossover Molecular Complexes, *Nanomaterials*, 2022, **12**, 1742.
7 A. Tissot, C. Enachescu and M.-L. Boillot, Control of the thermal hysteresis of the prototypal spin-transition $Fe^{II}(phen)_2(NCS)_2$ compound via the microcrystallites environment: experiments and mechanoelastic model, *J. Mater. Chem.*, 2012, **22**, 20451–20457.
8 F. J. Valverde-Muñoz, A. B. Gaspar, S. I. Shylin, V. Ksenofontov and J. A. Real, Synthesis of Nanocrystals and Particle Size Effects Studies on the Thermally Induced

Spin Transition of the Model Spin Crossover Compound $[Fe(phen)_2(NCS)_2]$, *Inorg. Chem.*, 2015, **54**, 7906–7914.

9 C. Bartual-Murgui, E. Natividad and O. Roubeau, Critical assessment of the nature and properties of Fe(II) triazole-based spin-crossover nanoparticles, *J. Mater. Chem. C*, 2015, **3**, 7916–7924.

10 C. D. Polyzou, E. Zygouri, N. Lalioti, O. Malina, M. Polaskova, J. Bednar and V. Tangoulis, Water stable colloidal PVP coated spin crossover nanoparticles, *Dalton Trans.*, 2024, **53**, 16821–16825.

11 M. Giménez-Marqués, M. L. García-Sanz de Larrea and E. Coronado, Unravelling the chemical design of spin-crossover nanoparticles based on iron(II)–triazole coordination polymers: towards a control of the spin transition, *J. Mater. Chem. C*, 2015, **3**, 7946–7953.

12 C. Etrillard, V. Faramarzi, J. F. Dayen, J. F. Letard and B. Doudin, Photoconduction in $[Fe(Htrz)_2(trz)](BF_4)\cdot H_2O$ nanocrystals, *Chem. Commun.*, 2011, **47**, 9663–9665.

13 Y. A. Tobon, C. Etrillard, O. Nguyen, J. F. Létard, V. Faramarzi, J. F. Dayen, B. Doudin, D. M. Bassani and F. Guillaume, Resonance Raman study of spin-crossover $[Fe(Htrz)_2(trz)](BF_4)\cdot H_2O$ particles coated with gold, *Eur. J. Inorg. Chem.*, 2012, 5837–5842.

14 A. Tokarev, L. Salmon, Y. Guari, G. Molnár and A. Bousseksou, Synthesis of spin crossover nano-objects with different morphologies and properties, *New J. Chem.*, 2011, **35**, 2081–2088.

15 A. Tokarev, L. Salmon, Y. Guari, W. Nicolazzi, G. Molnár and A. Bousseksou, Cooperative spin crossover phenomena in $[Fe(NH_2trz)_3](tosylate)_2$ nanoparticles, *Chem. Commun.*, 2010, **46**, 8011–8013.

16 T. Forestier, A. Kaiba, S. Pechev, D. Denux, P. Guionneau, C. Etrillard, N. Daro, E. Freysz and J. F. Létard, Nanoparticles of $[FeNH_2\text{-}trz_3]Br_2\text{-}3H_2O$ (NH_2-trz = 2-Amino-l,2,4-triazole) prepared by the reverse micelle technique: Influence of particle and coherent domain sizes on spin-crossover properties, *Chem.–Eur. J.*, 2009, **15**, 6122–6130.

17 H. Peng, S. Tricard, G. Félix, G. Molnár, W. Nicolazzi, L. Salmon and A. Bousseksou, Re-Appearance of Cooperativity in Ultra-Small Spin-Crossover $[Fe(pz)\{Ni(CN)_4\}]$ Nanoparticles, *Angew. Chem., Int. Ed.*, 2014, **53**, 10894–10898.

18 G. Bovo, I. Bräunlich, W. R. Caseri, N. Stingelin, T. D. Anthopoulos, K. G. Sandeman, D. D. C. Bradley and P. N. Stavrinou, Room temperature dielectric bistability in solution-processed spin crossover polymer thin films, *J. Mater. Chem. C*, 2016, **4**, 6240–6248.

19 C. Faulmann, J. Chahine, I. Malfant, D. de Caro, B. Cormary and L. Valade, A facile route for the preparation of nanoparticles of the spin-crossover complex $[Fe(Htrz)_2(trz)](BF_4)$ in xerogel transparent composite films, *Dalton Trans.*, 2011, **40**, 2480–2485.

20 A. Nakamoto, N. Kojima, L. Xiao-Jun, Y. Moritomo and A. Nakamura, Demonstration of the thermally induced high spin–low spin transition for a transparent spin crossover complex film $[Fe(II)(H\text{-}trz)_3]$-Nafion (trz = triazole), *Polyhedron*, 2005, **24**, 2909–2912.

21 Y.-X. Wang, D. Qiu, S.-F. Xi, Z.-D. Ding, Z. Li, Y. Li, X. Ren and Z.-G. Gu, Iron(II)-triazole core–shell nanocomposites: toward multistep spin crossover materials, *Chem. Commun.*, 2016, **52**, 8034–8037.

22 J. Dugay, M. Aarts, M. Giménez-Marqués, T. Kozlova, H. W. Zandbergen, E. Coronado and H. S. J. Van Der Zant, Phase transitions in spin-crossover thin films probed by graphene transport measurements, *Nano Lett.*, 2017, **17**, 186–193.

23 Y. Murashima, M. R. Karim, N. Saigo, H. Takehira, R. Ohtani, M. Nakamura, M. Koinuma, L. F. Lindoy, K. Kuroiwa and S. Hayami, Graphene oxide and reduced graphene oxide hybrids with spin crossover iron(III) complexes, *Inorg. Chem. Front.*, 2015, **2**, 886–892.

24 D. Qiu, D.-H. Ren, L. Gu, X.-L. Sun, T.-T. Qu, Z.-G. Gu and Z. Li, Spin crossover-graphene nanocomposites: facile syntheses, characterization, and magnetic properties, *RSC Adv.*, 2014, **4**, 31323–31327.

25 P. Gkolfi, D. Tsivaka, I. Tsougos, K. Vassiou, O. Malina, M. Polaskova, C. D. Polyzou, C. T. Chasapis and V. Tangoulis, A facile approach to prepare silica hybrid, spin-crossover water-soluble nanoparticles as potential candidates for thermally responsive MRI agents, *Dalton Trans.*, 2021, **50**, 13227–13231.

26 A. Regueiro, M. Martí-Carrascosa, R. Torres-Cavanillas and E. Coronado, Unlocking room-temperature bistable spin transition at the nanoscale: the synthesis of core@shell $[Fe(NH_2trz)_3(NO_3)_2]@SiO_2$ nanoparticles, *Dalton Trans.*, 2024, **53**, 8764–8771.

27 E. Coronado, J. R. Galán-Mascarós, M. Monrabal-Capilla, J. García-Martínez and P. Pardo-Ibáñez, Bistable Spin-Crossover Nanoparticles Showing Magnetic Thermal Hysteresis near Room Temperature, *Adv. Mater.*, 2007, **19**, 1359–1361.

28 R. Díaz-Torres, G. Chastanet, E. Collet, E. Trzop, P. Harding and D. J. Harding, Bidirectional photoswitchability in an iron(III) spin crossover complex: symmetry-breaking and solvent effects, *Chem. Sci.*, 2023, **14**, 7185–7191.

29 A. Tissot, L. Rechignat, A. Bousseksou and M.-L. Boillot, Micro- and nanocrystals of the iron(III) spin-transition material $[Fe^{III}(3\text{-}MeO\text{-}SalEen)_2]PF_6$, *J. Mater. Chem.*, 2012, **22**, 3411–3419.

30 R. Bertoni, M. Lorenc, A. Tissot, M. Servol, M. L. Boillot and E. Collet, Femtosecond spin-state photoswitching of molecular nanocrystals evidenced by optical spectroscopy, *Angew. Chem., Int. Ed.*, 2012, **51**, 7485–7489.

31 A. Tissot, Photoswitchable spin crossover nanoparticles, *New J. Chem.*, 2014, **38**, 1840–1845.

32 D. J. Harding, W. Phonsri, P. Harding, I. A. Gass, K. S. Murray, B. Moubaraki, J. D. Cashion, L. Liu and S. G. Telfer, Abrupt spin crossover in an iron(III) quinolylsalicylaldimine complex: structural insights and solvent effects, *Chem. Commun.*, 2013, **49**, 6340–6342.

33 N. Phukkaphan, D. L. Cruickshank, K. S. Murray, W. Phonsri, P. Harding and D. J. Harding, Hysteretic spin crossover driven by anion conformational change, *Chem. Commun.*, 2017, **53**, 9801–9804.

34 B. J. C. Vieira, L. C. J. Pereira, V. da Gama and J. C. Waerenborgh, Structural features that modulate the sharpness of the spin crossover transition in $[Fe^{III}(5\text{-X-qsal})_2]^+$ based salts, *CrystEngComm*, 2023, **25**, 6472–6477.

35 B. J. C. Vieira, L. C. J. Pereira, V. Gama, I. C. Santos, A. C. Cerdeira and J. C. Waerenborgh, Correlation between Supramolecular Connectivity and Magnetic Behaviour of $[Fe^{III}(5\text{-X-qsal})_2]^+$-Based Salts Prone to Exhibit SCO Transition, *Magnetochemistry*, 2022, **8**, 1.

36 K. Takahashi, K. Yamamoto, T. Yamamoto, Y. Einaga, Y. Shiota, K. Yoshizawa and H. Mori, High-Temperature Cooperative Spin Crossover Transitions and Single-Crystal Reflection Spectra of $[Fe^{III}(qsal)_2](CH_3OSO_3)$ and Related Compounds, *Crystals*, 2019, **9**, 81.

37 S. Hayami, K. Hiki, T. Kawahara, Y. Maeda, D. Urakami, K. Inoue, M. Ohama, S. Kawata and O. Sato, Photo-induced spin transition of Iron(III) compounds with π-π intermolecular interactions, *Chem.–Eur. J.*, 2009, **15**, 3497–3508.

38 H. Zenno, R. Hieda, R. Nakao, Y. Sekine and S. Hayami, Hidden spin state accessed by light irradiation in an iron(III) high-spin complexes, *Dalton Trans.*, 2025, **54**, 13426–13430.

39 M. A. López-Quintela, Synthesis of nanomaterials in microemulsions: formation mechanisms and growth control, *Curr. Opin. Colloid Interface Sci.*, 2003, **8**, 137–144.

40 M. A. López-Quintela, C. Tojo, M. C. Blanco, L. García Rio and J. R. Leis, Microemulsion dynamics and reactions in microemulsions, *Curr. Opin. Colloid Interface Sci.*, 2004, **9**, 264–278.

41 C. L. Kitchens, M. C. McLeod and C. B. Roberts, Solvent effects on the growth and steric stabilization of copper metallic nanoparticles in AOT reverse micelle systems, *J. Phys. Chem. B*, 2003, **107**, 11331–11338.

42 C. Tojo, M. de Dios and F. Barroso, Surfactant Effects on Microemulsion-Based Nanoparticle Synthesis, *Materials*, 2010, **4**, 55–72.

43 L. Zhang, J.-J. Wang, G.-C. Xu, J. Li, D.-Z. Jia and S. Gao, Tuning size and magnetic thermal hysteresis in a new near room temperature spin crossover compound, *Dalton Trans.*, 2013, **42**, 8205–8208.

44 J. Laisney, A. Tissot, G. Molnár, L. Rechignat, E. Rivière, F. Brisset, A. Bousseksou and M.-L. Boillot, Nanocrystals of $Fe(phen)_2(NCS)_2$ and the size-dependent spin-crossover characteristics, *Dalton Trans.*, 2015, **44**, 17302–17311.

45 F. Volatron, L. Catala, E. Rivière, A. Gloter, O. Stéphan and T. Mallah, Spin-crossover coordination nanoparticles, *Inorg. Chem.*, 2008, **47**, 6584–6586.

46 J. Sirirak, W. Phonsri, D. J. Harding, P. Harding, P. Phommon, W. Chaoprasa, R. M. Hendry, T. M. Roseveare and H. Adams, Halogen substituted quinolylsalicylaldimines: Four halogens three structural types, *J. Mol. Struct.*, 2013, **1036**, 439–446.

47 *CrysAlisPro*, Rigaku Oxford Diffraction, Rigaku Corporation, 2019, Rigaku Corporation:1.171.40.58a.

48 G. M. Sheldrick, SHELXT - Integrated space-group and crystal-structure determination, *Acta Crystallogr., Sect. A*, 2015, **71**, 3–8.

49 G. M. Sheldrick, Crystal structure refinement with SHELXL, *Acta Crystallogr., Sect. C:Struct. Chem.*, 2015, **71**, 3–8.

50 O. V. Dolomanov, L. J. Bourhis, R. J. Gildea, J. A. K. Howard and H. Puschmann, OLEX2: a complete structure solution, refinement and analysis program, *J. Appl. Crystallogr.*, 2009, **42**, 339–342.

51 CCDC 2491569: Experimental Crystal Structure Determination, 2026, DOI: 10.5517/ccdc.csd.cc2pmp67.